

Kevin EYSSARTIER

Étudiant 3^{ème} année PHELMA SICOM
Institut National Polytechnique de Grenoble
3, Parvis Louis Néel, BP 257 - 38016 Grenoble Cédex 01
Tél. : +33 6 19 11 13 38
Mail : Kevin.Eyssartier@phelma.grenoble-inp.fr

Dr Francisco Lopez-Dekker

DLR-Standort Oberpfaffenhofen
Deutsches Zentrum für Luft- und Raumfahrt
Münchner Straße 20 82234 Weßling
Tel.: +49 8153 28-0
Mail : Francisco.LopezDekker@dlr.de

Monitoring the Petermann Ice Island (2010) using TanDEM-X satellites

Abstract

In August 2010, the head of one of the biggest glacier on Earth, the Petermann glacier located in Greenland, broke into a 250km² Iceberg. It travelled at a fast pace into the Nares strait and turned into an ecological warning. The goal of this project was to study the evolution of this iceberg, and in particular to study the changing topography due to melting and calving using a time-series of TanDEM-X interferometric Synthetic Aperture Radar (SAR) image processing data. The main challenge to be addressed in the context of this project was the large scale motion of the glacier, including drifts (translation) and rotations, which had to be estimated and compensation in order to work on a reference system tied to the Iceberg. These challenges have been addressed combining techniques rooted in InSAR processing (such as block correlations) and Image Processing methods, such methods such as region growing, or the Radon transform. This presentation will describe in detail the processing flow, with an emphasis on steps not required in typical stacks processing, and present some preliminary results.

Introduction

The TanDEM-X (TerraSAR-X Add-On for Digital Elevation Measurements) mission of Earth surface monitoring has begun in end June 2010 shortly after the launching of the TanDEM-X (TDX) satellite. It has joined his twin, TerraSAR-X (TSX), which was already orbiting since January 2008 and was acquiring Synthetic Aperture Radar data by its own. Those two satellites are now flying in close formation in order to acquire single-pass interferometric SAR (InSAR) data with the goal of providing a global Digital Evolution Model (DEM) with $12 \times 12 \text{ m}^2$ horizontal sampling and 2 m vertical relative accuracy. The satellites are planned to fly within a less than a kilometre range but until October 2010 the TDX satellite was still in monostatic commissioning phase, and therefore was in the similar orbit but with a large along-track distance of 20 km, this induced a lag of a few seconds between the two acquisitions.

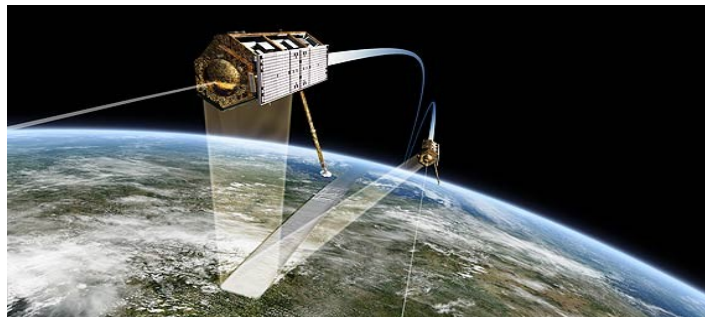


Figure 1. flying in formation, TanDEM-X and TerraSAR-X, artist view.

In August 2010, the Petermann glacier broke and created a iceberg named the Petermann ice island. The glacier is around 70 km long and 15 km large, located in the Greenland near the 81 degrees north latitude. The failure separated an approximately $25 \times 10 \text{ km}^2$ iceberg which is now drifting in the Arctic water, that is $1/4^{\text{th}}$ of the glacier surface but only $1/10^{\text{th}}$ of its weight as the glacier is much more thin at its end. Monitoring this moving iceberg became an interesting project to test and display the capabilities of the young satellites. A time-serie of inSAR data of the area has been taken between the 25th of August and the 19th of September 2010, it is during this time span that the Petermann ice island start drifting considerably into the Nares strait. The project's goal is to monitor the evolution of the iceberg, its drifting and rotation but especially its melting and calving. We will use the fine spatial and height resolution of the TanDEM-X mission to achieve this objective.

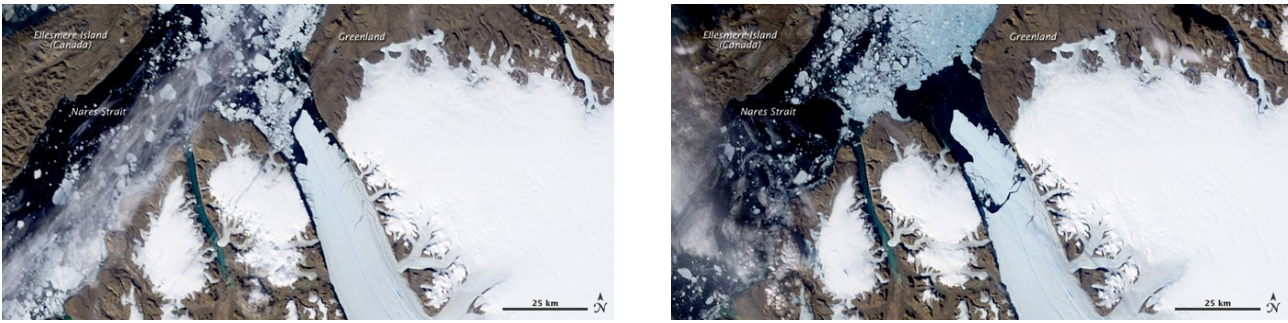


Figure 2. the Petermann glacier the 28th July 2010 (left) and the 5th August 2010 (right). Images in natural colors taken by the optical NASA's MODIS system [1].

The final objectives are to create a melting and carving time-series mapping and to animate it. This time-series should estimate the modifications on the surface through the different acquisitions. It is also required for this process to be reproducible so that following researcher could use this protocol for any iceberg, but also to be extended to other climates and usages. The first chapter of this report is composed by a brief description of the laboratory we worked in. To explain the full objective's implications, we will then in the second chapter talk about the methodology by describing all the technology and theories we could use in this project. As the spatial imagery domain is quite vast and complicate, we can describe the major problems we had to answer only after these theoretical explanations. In chapter three we will precisely explain our choices in the process, what are its flows and capacities and presenting the results.



Figure 3. The big Kahuna rift on the Petermann glacier in August 2009, separating the inland part of the ice shelf from a 150 km² future ice berg detachment. The photo is taken looking up glacier. The glacier front is to the right of the point of view. The freeboard height is around 30 m toward the middle of the ice shelf and thins gradually to 5-10 m where the ice meets the land.

Picture: Jason Box

Table of contents

| | |
|--|-----------|
| I. DLR – Obberpfafenhofen..... | 4 |
| <i>Microwaves and Radar institute.....</i> | <i>4</i> |
| II. Methodology..... | 5 |
| 1. <i>TanDEM-X.....</i> | <i>5</i> |
| 2. <i>Computer and programs.....</i> | <i>7</i> |
| 1. IDL | |
| 2. Server | |
| 3. TAXI | |
| 3. <i>SAR Imagery.....</i> | <i>8</i> |
| 1. General view | |
| 2. Geometric explanation | |
| 4. <i>INSAR specificities.....</i> | <i>12</i> |
| 1. General view | |
| 2. The interferometric process | |
| 3. Movement and distortion | |
| III. Realisations..... | 17 |
| 1. <i>Process.....</i> | <i>17</i> |
| 2. <i>Pre-processing.....</i> | <i>19</i> |
| 1. Area of interest | |
| 2. Removing fringes | |
| 3. <i>Estimation of the rotation.....</i> | <i>22</i> |
| 1. Radon process | |
| 2. Block correlation | |
| 4. <i>Surface monitoring.....</i> | <i>28</i> |
| IV. Conclusion..... | 30 |

I. DLR – Obberpfafenhofen

Microwaves and Radar institute

The institute has more than 80 years experience in radio frequency technology and has for more than 25 years been active in microwave remote sensing. It holds leading expertise in SAR system design, operation, data processing, air- and space-borne SAR interferometry and polarimetry, innovative SAR operation modes, processing and inversion algorithms.

In 2000 the institute participated in the SRTM mission with the leadership for the X-SAR project. One year later the SAR-Lupe project started consisting of a constellation of five high resolution SAR satellites operating in X-band. The Institute supports this project with technical consultancy in a number of system aspects, like mission planning, sensor performance estimation and simulation. A few months later the approval for the realisation of TerraSAR-X has been obtained. TerraSAR-X is the first German radar satellite realized under a Public Private Partnership between DLR and EADS Astrium GmbH and launched in summer 2006. Within the TerraSAR-X project the Institute is delivering system engineering support, holding the mission manager position and developing the Instrument Operations and Calibration System.

Building on the experience gained in more than 25 years with the successful participation in NASA's Shuttle Radar Programme and the TerraSAR-X mission, the Institute submitted in November 2003 the TanDEM-X mission proposal that was finally accepted in March 2006 following a successful demonstration of its feasibility during the phase A study. TanDEM-X has the objective to generate a consistent, global Digital Elevation Model with an unprecedented accuracy. This goal will be achieved by means of a second slightly modified TerraSAR-X satellite flying in a close orbit formation with TerraSAR-X. TanDEM-X has been launched in June 2010 and is the first spaceborne bistatic radar system and the first operational close formation flying system in space. In addition to across-track interferometry, TanDEM-X will allow the demonstration of several new techniques and modes like digital beamforming, super resolution, single-pass polarimetric SAR interferometry, four phase-center along-track interferometry and others.

The Institute participated in the last years in a number of ESA projects and has developed a close cooperation with the German space industry. It contributes actively to several new satellite programmes such as ALOS/PALSAR, MAPSAR, Sentinel-1, SMOS, BIOMASS, COREH2O, and TANDEM-L.

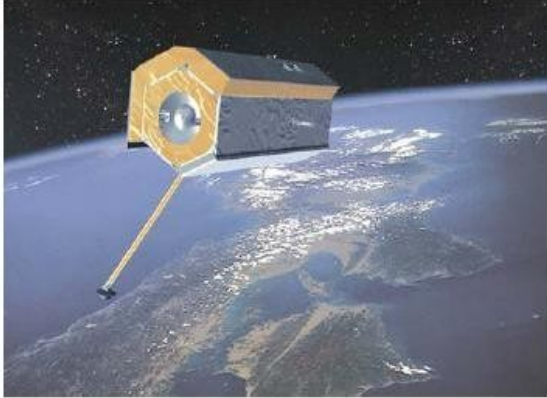
II. Methodology

In this section we will describe the equipments and the theories we could rely on during this internship. All the data we could study was taken by the TanDEM-X satellites which we will first describe. Then comes the office's hardware facilities, which consist of server, Idl programming language and TAXI. Finally, we will outline the main principles of the SAR imaging and the SAR interferometry especially the theoretical characteristics we had to keep in mind during the project.

II.1. *TanDEM-X*

All the data processed during this project are taken from the TanDEM-X (TerraSAR-X add-on for digital evolution model) mission. This missions is composed of two nearly similar satellites, TerraSAR-X (TSX) and TanDEM-X (TDX). The TSX satellite is orbiting the Earth since June 2007, TDX has been launched in June 2010. The TanDEM-X mission is a joint project between the German Aerospace Center (DLR) and the German industry (ASTRIUM). The TerraSAR-X instrument is a side-looking X-band synthetic aperture radar (SAR) based on activephased array antenna technology. Figure 4. shows an artists view of the satellite and the tables summarizes the characteristic values of the platform and the SAR instrument. In June 2010, TSX was supplemented in orbit by its twin, the TDX instrument. In a close formation flight, they will separately acquire data for the TerraSAR-X mission and jointly execute the TanDEM-X mission data collection. With the finalization of its monostatic commissioning phase in October 2010, it could be confirmed that the second satellite will provide the SAR data for the TerraSAR-X mission with nearly identical performance parameters and stability as the first one. Those two twin satellites are orbiting with helicoïdal trajectories that have to be drastically controlled. [2]

The TanDEM-X mission main goal is to map the whole earth surface with high resolution digital evolution model (DEM). TDX has joined the TSX orbits 2 days after its launch, the 21st of June 2010, and sent its first image the 23rd. The system composed by the two satellites describe a full circle around the earth in 95 minutes. And due to its high inclination of 97.44° it fly over the same area every 11 days. To circumvent this time problem, the satellite's antennas can rotate with different angles, that allow them to fully cover the previous footprints despite a different point of view. Our data in this project are acquired from five different points of view. This is important since the SAR imaging process is displayed in the range and azimuth direction with a different resolution for each axe. This would result into unstackable pixels. Another problem resulting from this multiple points of view is the times of acquisition. The different points of view are not all acquired at the same time of the day and this can have a strong effect. Indeed, the signal is not necessarily echoed by the first material obstacle, it penetrates the obstacle depending of its constitution and materials properties. If the acquisition is taken during day time, it is highly probable that the signal will go through more soften icy layers than during cold night. We had no solution to correct this, we should keep in mind this unsolvable artefact.



| Orbit and Attitude Parameters | |
|---|---------------------------------|
| Nominal orbit height at the equator | 514 km |
| Orbits / day | 15 ² / ₁₁ |
| Revisit time (orbit repeat cycle) | 11 days |
| Inclination | 97.44° |
| Ascending node equatorial crossing time | 18:00 ± 0.25 h (local time) |
| Attitude steering | "Total Zero Doppler Steering" |

| System Parameters | |
|--|---|
| Radar carrier frequency | 9.65 GHz |
| Radiated RF Peak Power | 2 kW |
| Incidence angle range for stripmap / ScanSAR | 20° – 45° full performance (15°-60° accessible) |
| Polarizations | HH, VH, HV, VV |
| Antenna length | 4.8 m |
| Nominal look direction | right |
| Antenna width | 0.7 m |
| Number of stripmap / ScanSAR elevation beams | 12 (full performance range) 27 (access range) |
| Number of spotlight elevation beams | 91 (full performance range) 122 (access range) |
| Number spotlight azimuth beams | 229 |
| Incidence angle range for spotlight modes | 20° – 55° full performance (15°-60° accessible) |
| Pulse Repetition Frequency (PRF) | 2.0 kHz – 6.5 kHz |
| Range Bandwidth | max. 150 MHz (300 MHz experimental) |

Figure 4. Artists view of TerraSAR-X, Orbits and system parameters of TerraSAR-X.

The instrument timing and pointing of the electronic antenna can be programmed allowing a numerous combinations. Four imaging modes are designed to support a variety of applications ranging from medium resolution polarimetric imaging to high resolution mapping. Only the Stripmap mode has been used for this project. During a Stripmap acquisition, the beam keep a constant angle which allow a non-stop measurement. On the other hand, the three other achieve a higher 3-D resolution due to a rotating beam that acquire more data from the same footprint. This mode has been chosen has it is the only mode that can acquire a moving object over its flypath despite its lower resolution.

The failure of the Petermann glacier happened during the pursuit monostatic commissioning phase, that means that some adjustment in the acquisition protocol were impossible. The commissioning phase is the time when both of the satellites have still not reach their final positions. They are on the good orbits but still distant from 20km, compared to the 200 or 500m during their full time mission, that leads to some limitations. First of all, the acquisitions were forced to a monostatic mode, which defined the way data is captured. In monostatic acquisition each satellite send and receive a signal by its own. The bistatic acquisition, which is the planned main type of acquisition for the mission, is defined when one satellite emits for both of them to receive. This acquisition mode improves drastically the accuracy of the further

interferometric process. Indeed, it allows a substantial power reuse but also a reduction of temporal decorrelation and atmospheric disturbances. Prerequisites for this bistatic are the Pulse Repetition Frequency (PRF) synchronisation based on GPS as a common time reference and the relative phase reference between the two satellites.[3] Moreover, this 20km distance forced a lag of 3 seconds between the acquisitions which is relevant in a motion tracking utility. This time difference will impact directly our work and should be taken with careful considerations.

II.2. Computer and programs

In this part we we will describe the ground equipments which are mainly the computer language, the server architecture and the TAXI program. The language used during this project is IDL, this is quite obvious as this is the language almost every spatial centre are working with. The server architecture is somewhat trivial, but it is nonetheless important to underline the huge computing capacities InSAR imaging requires. Finally we will describe the TAXI (experimental **T**anDEM-**X** Interferometric processor), which is a DLR made program providing an easy and versatile processing of InSAR images.

II.2.1. IDL

The Interactive Data Language (IDL) is a programming language used for data analysis. It is essentially used in astronomy and medical imaging as it is a vectorized and interactive language, comfortable with processing large amounts of data. The IDL was developed in the 1970s at the Laboratory for Atmospheric and Space Physics at the University of Colorado. It has tremendously improved since then and it now deals with more complex computing. IDL is widely used in the space science, it has processed all the Halley comet pictures of the European Space Agency and is also dominant in the DLR and NASA space imaging works. Its syntax is quite similar to the Matlab one and it is also a vector programming language so that every function has to be programmed using the vector implementation of the built-in functions: every explicit loop should be avoided.

II.2.2. Server

The Microwaves and Radar Institute's server architecture rely on multiple computing servers. The one we used in this project is the ophrlx02 server, its central processing unit contains eight AMD Opteron Modell 8360SE which are 2.5GHz quad core processing units that means a 32 multi-core processor. It obviously contains huge data storage (around 20TB) in order to deal with the huge amount of data. For example each InSAR couple we processed is approximately 4GB and took 3 days to process with the non-improved data. Such high speed computing and large storage technologies are required for the long and arduous SAR and InSAR imaging process, as we will see in the theoretical parts.

II.2.3. TAXI

TanDEM-X is the first bistatic SAR mission in space. As it is widely recognised, bistatic SARs offer increased performance at an increased operational cost. For the evaluation of the TDX experiments, the TAXI's flexible interferometric chain was developed at the Microwaves and Radar Institute of DLR to exploit

the novel scientific data that will be gathered during the mission. TAXI is a versatile SAR processing chain mainly composed of three main branches: a) a high-precision spaceborne monostatic part for the processing of TSX data, b) a high precision spaceborne bistatic part for the processing of TanDEM-X data, and c) an interferometric part for the combination of a stack of images, including the steps of DEM generation and geocoding [4]. All these steps will be discussed in the InSAR process description (II.4.2). The flexibility in the implementation of TAXI eases the extension and integration of new modules, hence becoming the perfect platform to process and evaluate new and challenging experiments.

II.3. SAR Imagery

It is necessary to describe SAR imagery before going to interferometry. As SAR is not our main point in this project we will only describe the basics, the not essential parts will be omitted.

II.3.1. General view

The Synthetic Aperture Radar is composed of a single looking beam-forming antenna mounted on a moving space or air shuttle, TandemX in our case. The target scene is continuously illuminated by emission of pulse of radio waves. The echoes received by the antenna are stored and post-processed to obtain precise spatial resolution. This technology has two main differences with optical imagery which will be important for the next:

- SAR is an active instrument. It generates its own coherent illumination of the scene to be viewed. A SAR instrument can measure both intensity and phase of the reflected light, resulting not only in a high sensitivity to texture, but also in some three-dimensional capabilities.
- SAR uses microwave frequency radiation. It penetrates cloud and haze, so SAR views the Earth's surface (land and sea) in all weather.

SAR imaging is a radar method and therefore it is a two steps procedure. The raw data are acquired by a coherent radar, then they are processed to form an image (called "focusing"). Those processing can be challenging due to the non-stationnarity of the operations, hence it is still a challenge for real time or on board implementations.

II.3.2. Geometric explanation

A spaceborne or airborne SAR illuminates the Earth's surface in a side-looking fashion. While the sensor is moving along the path (considered straight) at an altitude H above (x,y) it transmits microwave pulses into the antenna footprint at the pulse repetition frequency and receive the echoes from each pulses (*fig.5*). The SAR receiver detects and separates the stream of coherent echoes into individual echoes. Wavelength usually used are 3cm (X-band), 6cm (C-band), 9cm (S-band) and 24cm (L-band).

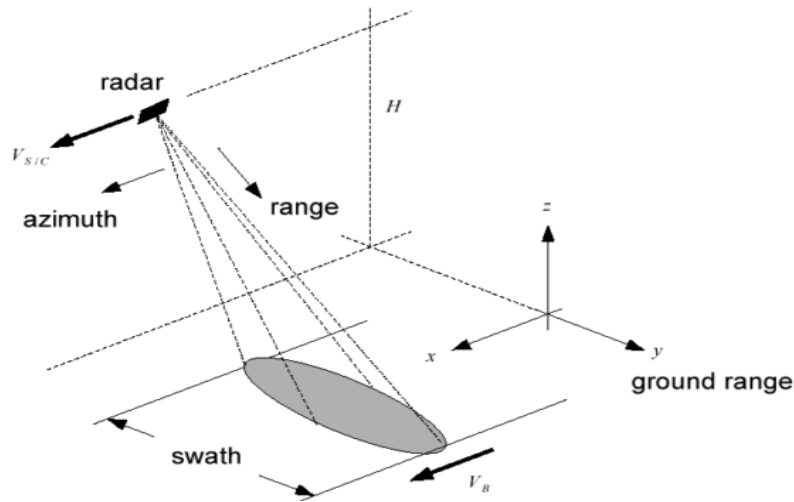


Figure 5. SAR imaging geometry. x is frequently called 'along-track' or 'azimuth', y is the 'ground range'.

The first problem encountered when dealing with radio waves observation is the resolving power of the antenna. The resolving power of an antenna with a diameter D at a wavelength λ is given by the ratio λ/D , that means that two objects separated by a distance X and observed by a range R will only be seen if the ratio $X/R > \lambda/D$. Thus, the smaller resolving power is the more details we will get. The pupil of the human eye is 3mm aperture and is collecting wavelength about $0.3\mu\text{m}$ which gives a resolving power of $1/6000$: it can distinguish two objects 1m apart at a range of 6km. The largest antennas that can be deployed in space are 15m, but as we saw they use radiation in the centimeter range. TerraSAR-X's carrier frequency is 9.65GHz (3.1cm wavelength), its antenna is 4.8m and it flies at 514km at the equator. Therefore we can resolve two points if their distance is more than $R * \lambda/D = 3.3\text{km}$. To overcome this difficulty and create sufficiently detailed images (meaning with a resolution of a few meters) we apply techniques specific to each direction in the image which restore adequate resolution.

The first technique is called 'range vision', it takes advantage of the fact that the instrument is active so that we can measure the round-trip time between the radar and the observed region. We can therefore distinguish between two points whose radar range differ by a few meters as long as the pulse duration is sufficiently short and the sampling rate of the echo is sufficiently high. Thus the sampling frequency in range f_d defines the size of the range pixel p_d by

$$p_d = \frac{c}{2 f_d \sin(\gamma)} \quad (1)$$

where the factor 2 takes account of the fact that the difference between two pixels includes the round trip. This relation take also into account the incidence angle γ , it explains why the instruments must be side-looking so that the ground distance of a point from the nadir of the radar can be sorted as a function of its range from the radar. On the figure 6 we have the distance p_d which is equal to the distance between a' and b' .

The problem with this technique is that it produces geometric distortion in the case of steep surface relief, many point will be processed as part of the same range distance. On the left diagram of the figure 6,

all the point between a and b will be compacted into a' and b' whereas the points between b and c will be dilated into the b'c' segment. That will result in an error in amplitude: the a'b' segment will be very bright due to the higher energy it will receive, but also an error in location (*fig.6 right diagram*)

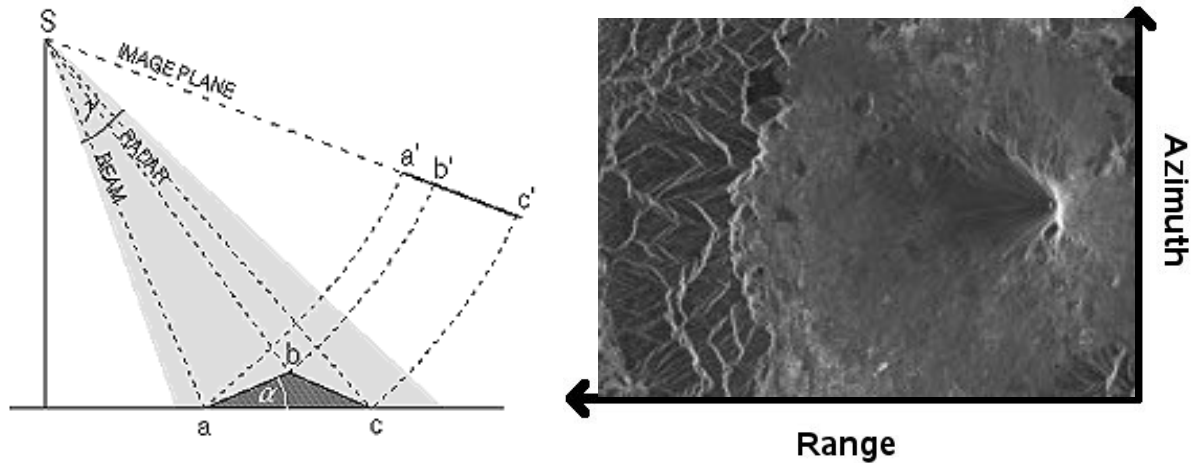


Figure 6. Example of range distortion, all the points between a and b will be considered nearer than it should. On the left picture, an example of this distortion, Mount Fuji observed by COSMO-Skymed

The second technique is the 'SAR synthesis'. During his acquisition the radar sends and catches multiple trains of pulse. Thus the same point in the footprint is illuminated a number of time depending to the pulse repetition frequency f_a , the speed of the spacebourne radar v and the width of the illuminated region L . In case of a non-zero curvature velocity of the satellite the relationship is more complicated, with Kepler's law a good approximation of the size of the azimuth pixel p_a is

$$p_a = \frac{C_{earth}}{T_{orb} f_a} \quad (2)$$

where T_{orb} is the orbital period and C_{earth} is the circumference of the Earth. Now let us assume that the radar transmits a pulse each time it travels the distance p_a . The target point A of the footprint is illuminated by L/p_a pulses which imply that A contributes to each of these pulses by returning an amplitude and a phase. Each pulse to which A contibutes will have approximately the same amplitude because the angle with which A is observed vary little due to the low ratio L/R . But the phase will vary with the distance between the point and the radar position. One easy solution is to modify the phase of the samples to which the target A has contributed, so that they all have the same phase, and then to add all the samples together. If they are all added when in phase, the samples will reinforce each other. However, each of these samples also includes, for a width of ground L , the contribution of the other targets. Let's take for example the target B which is separated from A by the distance p_a , B is the closest point to A that we want to distinguish from A. Taking into account the round-trip and the phase compensation used to favor target A, the phase values of B will be regularly distributed and therefore will cancel out by the addition. However, B contributions will be cancelled only if the maximum distance offset reach a quarter of a wavelength (that

is one half wavelength in round-trip) so that we can have all the phases cancelling each other. That gives us the limitation for p_a ,

$$p_a \geq \frac{\lambda R}{2L} \quad (3)$$

What are the limitations of this technique? At some point, the offset will add half a wavelength between each sample. For a round-trip, the phases will therefore be the same as for the target A, because a complete phase cycle does not change the signal. This is why the footprint, and therefore L, must only contain targets which are within a $\lambda/2$ phase offset. That gives us the relation

$$p_a \leq \frac{\lambda R}{2L} \quad (4)$$

If we consider an antenna of length D illuminating a region whose width is L. We know that the wavelength λ and the observation range R are related by

$$\frac{\lambda}{D} \approx \frac{L}{R} \quad (5)$$

By combining the equations (4) and (5) we then have

$$p_a \approx \frac{D}{2} \quad (6)$$

A pulse must be transmitted every time the radar travels a distance equals to one half of the length of its antenna. The resolution in the azimuth direction is therefore equal to $D/2$, this is contrary to everything we know about antenna resolution because in this case the smaller the antenna, the better the resolution. Surprisingly, the resolution is not dependent of the observation range. But there is a price to pay for this strange phenomena, in this case it is the amount of processing needed. We need to change L/p_a phases before adding them, that means around 1400 phase shifts in the case of TerraSAR-X for each point on the image. For memory, this radar has a resolution which is around 3m x 3m and have acquisitions that can be of thousands of square kilometre. [5]

The third point we want to describe is the speckle noise . The coherent nature of radar illumination causes the speckle effect, which gives the SAR image its noisy appearance. For example, let us imagine a natural fairly 'regular' surface so that the human eye would perceive it as a regular surface. Seen by a radar, each image pixel from this surface contains a large number of elementary scatterers, which add their contributions to the electromagnetic field radiated by the pixel in a coherent way. The total pixel response in amplitude and in phase is the result of vector addition of these contributions in the complex plane. Even though adjacent pixels are created by similar conditions at a macroscopic scale, their internal structures at

the scale of a wavelength (a few centimeters) differ enough to result in independent phase rearrangements. Differences in range as small as $\lambda/4$ reshuffle the phases between scatterers. This mechanism is not random but is unpredictable and will later be assumed to be a multiplicative noise. Basically it is assumed that the number of scatterers inside the resolution cell is large enough to fulfill the central limit theorem, so that the real and imaginary parts of a distributed target have a Gaussian zero-mean model.

Since speckle is often modelled, for single SAR imagery, as a multiplicative random noise process statistically independent of the scene, it can be reduced through an averaging process in order to obtain a better estimation of the desired information. This process is commonly known as multilook. The drawback is, of course, the resolution loss due to averaging. Multilook can be applied both in frequency or signal domain. The former consists in dividing the spectrum, either one-dimensionally or two-dimensionally, in separate looks, to later incoherently add the resulting images. The latter consists in applying an averaging window in signal domain.[6]

Now that we saw the range processing, that can cause spatial deformations, the SAR synthesis relying on phase distribution and the speckle noise, which reduces the resolution, which are the three main points of the SAR imaging technique, let us display the theory basis of the interferometric SAR and the problems and limitations we will have to deal with.

II.4. *INSAR specificities*

InSAR is the synthesis of conventional SAR imagery and interferometry techniques developed in radio astronomy. The use of SAR interferometers became popular only recently despite the fact its principle is known since the 1970s by Graham [7]. He added an additional physical antenna to a conventional airborne SAR system. This antenna was in the cross-track plane from the conventional antenna. By mixing the signals from the antennas, Graham recorded the first SAR interferometric signals. This has opened entirely new applications. The first published results in the view of terrestrial applications was in the 1980s [8][9]. After the launch of the ESA satellite ERS-1 in 1991 a lot of SAR data sets became available for interferometry and the method began to be investigated by many research groups.

InSAR developments in recent years, in part due to the active research of the German Aerospace Center (DLR) Microwaves and Radar Institute, have solved many of the limitations of the SAR systems and therefore allow projects of such a technical skill. Nowadays the SAR interferometry is an extremely powerful technique for mapping Earth surface topography. Many spaceborne SAR systems from several countries are regularly generating data [10]. Examples of such applications include land mapping, vegetation and biomass measurements and as for now polar ice research. In this chapter we will describe the basics of SAR interferometry, especially how we can extract the data we need for this project. We will also review the qualities and drawbacks of interferometry.

II.4.1. General view

A conventional SAR system is resolving targets into the range direction. We saw in the last part that SAR imaging collapses the three-dimensional world to two dimensions which are range and azimuth. To obtain the three-dimensional information an additional measurement of elevation angle is needed. If we

consider the situation shown in *fig. 7*, knowing the range r_1 and r_2 allow us to obtain the height h of the target by solving the parallax. The two acquisitions are distant by the baseline B with a certain angle α .

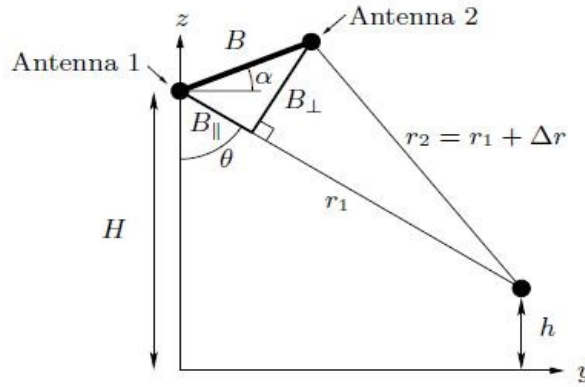


Figure 7. Sketch of SAR interferometry geometry

The Al-Kashi formula asserts that

$$r_2^2 = r_1^2 + B^2 - 2r_1 B \sin(\theta - \alpha) \quad (7)$$

$$B_{\parallel} = B \sin(\theta - \alpha) = \frac{r_1^2 + B^2 - r_2^2}{2r_1} = \{ r_2 = r_1 + \Delta r \} = \frac{B}{2r_1} + \frac{\Delta r^2}{2r_1} - \Delta r \approx -\Delta r \quad (8)$$

We defined here the *parallel baseline*. It is assumed that the range distance is much higher than the baseline. Once we know θ we can simply obtain the height of the target with

$$h = H - r_1 \cos(\theta) \quad (9)$$

Of course to estimate θ we must know Δr with a high precision. This is where the phase difference come into play. Considering that the phases for the two images of the same resolution cell are

$$\phi_1 = \frac{-4\pi}{\lambda} r_1 + \phi_{\sigma,1}$$

$$\phi_2 = \frac{-4\pi}{\lambda} r_2 + \phi_{\sigma,2} \quad (10)$$

respectively, an interferogram can be formed by multiplying one image with the complex conjugate of the second one. Assuming that both reflectivity are the same, the Hermitian product yields (omitting decorrelation terms)

$$\Phi_{interferometry} = \frac{4\pi}{\lambda} \Delta r \quad (11)$$

Now, the accuracy in the measurement of Δr is related to the accuracy in the measurement of the phase [11].

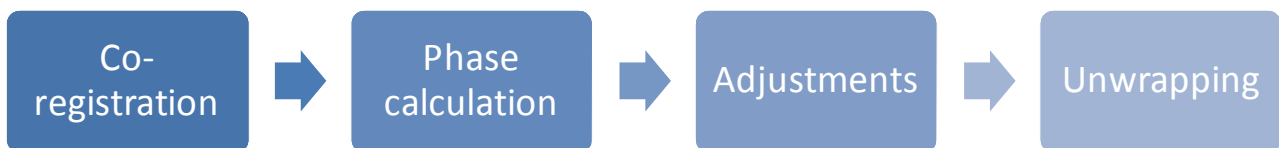
$$\sigma_{\Delta r} = \frac{\lambda}{4\pi} \sigma_{\phi}$$

$$\sigma_h = \frac{\partial h}{\partial \Delta r} \sigma_{\Delta r} = \frac{-r_l \sin(\theta)}{B \cos(\theta - \alpha)} \sigma_{\Delta r} = \frac{-r_l \sin(\theta)}{B \cos(\theta - \alpha)} \frac{\lambda}{4\pi} \sigma_{\phi} \quad (12)$$

That leads us to define the height of ambiguity. The height of ambiguity is the altitude gained if the phase is increased by 2π . It is indeed the factor that allow a higher altitude accuracy mapping. It is mostly dependant on the perpendicular baseline, the inclination of the beam and other acquisition dependent parameters (coherence, speckle noise, etc.). The height of ambiguity is the best indicator of the altitude accuracy.

II.4.2. The interferometric process

The full interferometric process is composed of four main steps.



1. The first step is the co-registration. This phase consist of modelling very precisely the geometrical differences between the two images, even at a sub-cell level, which implies that matching between corresponding pixels must be almost perfect. One of the images has to be stretched so that it can be registered on the other. Those operations must conserve the phase content otherwise a bias would be introduced in the interferometric measurements [12].

One possibility to estimate the offsets between images is by means of a coherence maximization procedure It consists in dividing both data sets in several patches to find both the azimuth and range offsets between these individual patches. The offsets that give the best coherence are used.

Afterwards, the result can be interpolated in order to have the offsets for each pixel of the image. When the images are quite decorrelated, the offset estimates can be very noisy. In this case, the normal procedure is to use only the cross-correlation of the amplitude or the intensity. Knowing the precise orbit timing are really helpful for this step [13].

2. The second step is the phase calculation which we had described in the first part of this section.
3. The adjustments consist of removing artefacts due to the previous steps of computations. It is necessary to filter it to reduce the phase noise coming from different sources: white noise, misregistration, possible temporal decorrelation, frequency shift to the relief, etc. We will not go further into details about this technical part, the important thing to remember here is that the phase calculation will not directly grant access to the wrapped DEM. However one point has to be noticed, the geometry between the inclination of the satellite during the acquisition and the relief of the target alters the result of the InSAR process. In order to remove this artefacts, we need to have a rough altitude map of the target and the precise orbit position at the time of acquisition. DEMs production at the DLR used to rely on the SRTM (Shuttle Radar Topography Mission) height maps, this NASA mission occurred in 11 days in February 2000 and its objective was to generate the most complete digital topographic database of Earth with InSAR. Its resolution is around 90x90 meter, compared to the 10x10m of the TDX mission. Unfortunately, the SRTM mission was constrained to 56°S to 60°N, therefore the Petermann Ice Island is out of the acquired area. For this mission we had to use a flat-earth model as the altitude map, implying that every important relief will give mistakes. It was assumed that the relative flatness of the Iceberg will limit this problem.
4. Finally the phase unwrapping which resides in extracting the altitude from the phase, that we can consider as a modulo of the altitude time a ratio. The phase of the interferogram contains now all the information we want but it is wrapped into the $[-\pi;\pi]$ interval and only the absolute phase is relevant for the altitude. Hence we need here an unwrapping algorithm. The algorithms used by TAXI are the *weighted least mean square – region growing* (WLMS-RG) and the SNAPHU algorithm [14].

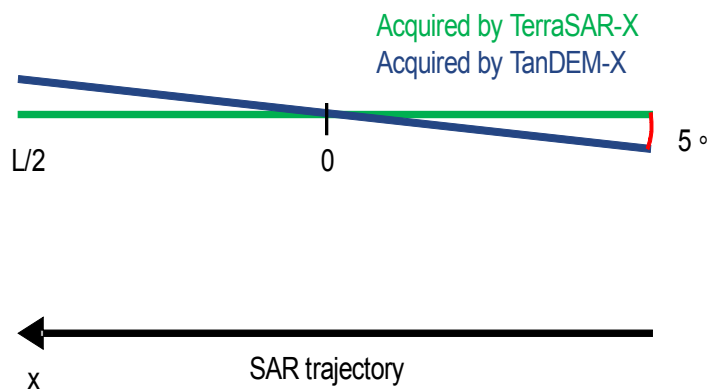
The WLMS approach is used to obtain a first (global) estimation of the unwrapped phase, by finding the minimum distance between the instantaneous frequency of the wrapped and unwrapped signals. The mask applied during WLMS is obtained by means of a first use of the region growing algorithm with a low coherence threshold. After a few iterations with WLMS (typically 5) the unwrapped phase is subtracted to the original phase modulo 2π . The residual phase is then unwrapped using again region growing. Since the low coherence threshold is used, the areas where region growing cannot enter are interpolated. To obtain the estimated unwrapped phase, both solutions, WLMS and region growing, are added [15].

The SNAPHU (Statistical-Cost, Network-Flow Algorithm for Phase Unwrapping) algorithm is using a more statistical way with the help of neural network techniques instead of the straight forward WLMS-RG method. For this project we used only the WLMS-RG algorithm because of the major low coherence region on our data.

II.4.3. Movement and distortion

In this part we will try to describe some of the effects of a moving target over SAR and InSAR imaging. First of all let us study the effect of translation on the SAR acquisition. If the target is moving in the azimuth direction, a problem due to the *SAR synthesis* (cf. Part II.3.2) will occur. Indeed, if the speed of the target is fast compared to the speed of acquisition (basically the speed of the space or airborne radar) the target will be seen with a slanted phase distribution and therefore be dislocated. Fortunately this has very few chance that this happen with the TDX satellites which are describing a full circle around the earth in ~ 90 minutes which correspond to a roughly speed of $8\text{km}\cdot\text{s}^{-1}$. Only target with at least a $10\text{m}\cdot\text{s}^{-1}$ in azimuthal direction will be disturbed by one pixel. This issue is most likely to happen with airborne system where the speed is significantly lower.

However displacement affects much more InSAR imaging. As the interferometric process rely on the phase of the signal and that the wavelength is around 3cm, every small movements are spotted by InSAR. A whole phase cycle will be added for each distance shifting of $\lambda/2$ which is roughly 1.5cm in our case. Let us consider a rotation along a vertical axis occurring during the interval between the acquisitions, as described in the following figure. We can see here that this displacement results in a linear modification, in the case of a rotation, an artificial slope in the azimuthal direction will be added. Even in the case of a drifting in the range direction, all the points of the target will be seen with a Δr offset and therefore seen with an altitude offset. This can be very problematic during the DEM production, the phase unwrapping can lead to strange results.



$$\phi_{interferometry} = \frac{4\pi}{\lambda} \Delta r = \frac{4\pi}{\lambda} x \tan(5^\circ) \quad (13)$$

With the average TDX parameters (1.8m azimuth pixel spacing, 3cm wavelength and an incidence angle of 45°) a rotation of just 0.7° between the two acquisition would cause a frequency of 1 cycle/sample, thus causing total decorrelation [16]. The InSAR acquisition process is therefore highly sensitive to even very small displacement, with a span of 3 seconds in capturing moving iceberg we should in all likelihood get displacement aberrations.

III. Realisations

In this section we will first discuss the approach we considered on the subject, describing the global meaning of the process. We will put special emphasis on the logic and the reasons that lead to this final algorithm. In this part we will also have a glance on the data, explaining the limitations and thus our choices. Then, in the second and third parts, we will deal with the functions one after the other in a more precise manner.

To describe the whole implemented process we will first describe the steps before the TAXI unwrapping, the post process steps and finally the monitoring and its results. The pre-processing steps are mainly how we can adapt the deficient InSAR images in order to generate proper DEMs. TAXI then perform the phase unwrapping on the processed data and generate the DEMs. The post-process steps consist of the evolution monitoring and how we can extract those informations from heterogeneous DEMs.

III.1. Process

In order to identify the movements and modifications that occurs on this iceberg, we have been given ten pairs of SAR images, each depicting a roughly 70x20km² area. These data cover the surfaces as seen on *fig. 8*, it represents the footprints from the different acquisitions. As we could not wait eleven days between each acquisition, the points of view and the angles of observation are different, this is thanks to the capabilities of the TanDEM-X mission. The first thing to do was to perform a standard inSAR processing on each pair of SAR images with Taxi (back-geocoding, interferometric process and co-registration) but stopping the usual process before the phase unwrapping, it is indeed the step where the characteristic artefacts on our data compromise the result. We now have ten InSAR images that consist of ten amplitude, phase and coherence images at ten different dates (cf *fig. 9*).

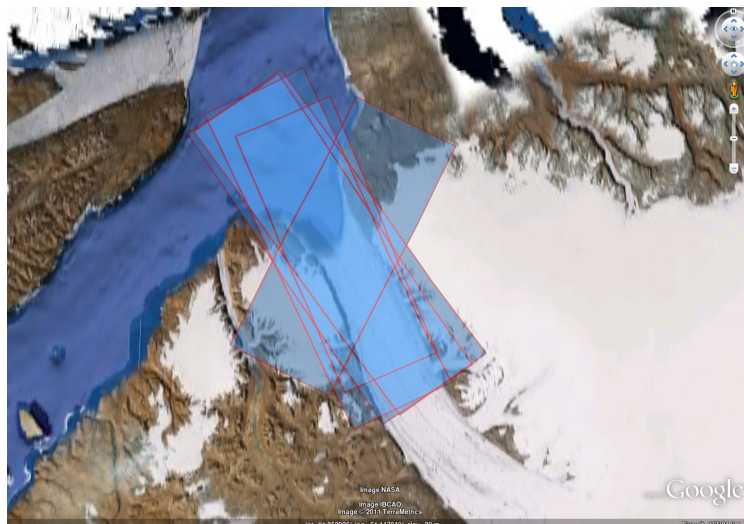


Figure 8. the five footprints of acquisition

As we saw in the theoretical part on Synthetic Aperture Radar, SAR imaging and SAR interferometry is problematic on a moving and incoherent surface. Consequently it is a hard task to process automatically an iceberg, it moves in three dimensions and it is surrounded by incoherent non-stationary water. On the *fig. 9* we have an example of the raw phase of the inSAR image still affected by rotational fringes. The first problem was the fringes in the azimuth direction that lead to huge aberrations during the DEM unwrapping. Those fringes, due to the rotation of the ice, had to be removed before the TAXI's DEM production take place. The second problem was how to deal with the surrounding water. First it leads to an enormous lost of time in the phase unwrapping computation due to its inconsistency: the unwrapping algorithm try by neighbouring to find some sort of continuity in the noise. For example, running an unwrapping on a full size image with water took three days even on the 32 processors of the server. Moreover the unwrapping is slow but it is also almost totally worthless as the water processing gives no information at all in our case. Secondly, in all DEMs the heights are relative: we cannot directly obtain the height of a surface surrounded by an incoherent region if we don't have a reference point on that surface. As we do not have any calibration point we could not access the altitude of the surface, only a relative height model. Besides the iceberg drift add an altitude offset on the whole target (cf Movement and distortion of InSAR II.4.3). Thus, before applying the unwrapping process we had to isolate the iceberg in order to remove as water as possible and then discard the vertical fringes.

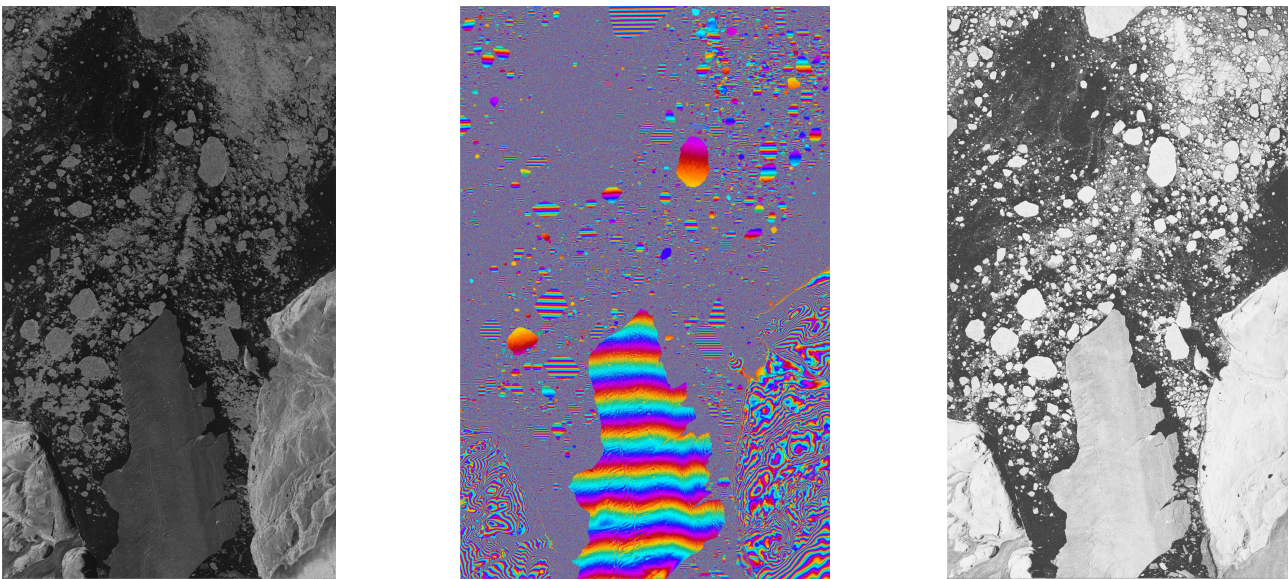


Figure 9. On the left: amplitude of the inSAR signal. In the middle: phase of the inSAR signal on the Petermann glacier. On the right: the phase coherence. Those images are in slant range azimuth (top to bottom) coordinates. The horizontal fringes and the noise of the water are clearly visible on the phase data.

With our refined data we can now run the Taxi program without enduring strange misconceptions. As our data are quite original we had to specify special options. As the point of view are different, the images are referenced in different coordinates: azimuth and range directions do not correspond. Moreover the range and azimuthal directions do not share the same resolutions, as a result the image's pixels were not square. So we had to specify to compute the images into geocoded coordinates so that the referential axes are the same for all the pictures and the pixels to be square.

Once we have the DEMs, we now try to estimate the melting on the iceberg surface. We possess ten geocoded DEMs of the area, spread on three weeks of acquisitions. Each of them is displaying the moving iceberg at a different time, thus we have to align the iceberg in order to perform the monitoring. The alignment is composed of two main steps, first we rotate the image so that they are facing the same direction, then with a cross correlation the image is translated in the right place. Those were quite difficult due to the large amount of data for each image and the evolution of the iceberg which disturb the alignment.

We now have geocoded DEMs which are fully stackable. The last step deals with the actual evolution monitoring. Here is the flow chart of the whole process:



Now that the whole process chain is roughly presented, we will describe with care the functions implemented to operate this process.

III.2. Pre-processing

III.2.1. Area of interest

As we explained, the first step in order to pre-process the data was to apply a segmentation algorithm to isolate the glacier, two solutions were considered. The first one is to rely on the phase vertical fringes to separate the pieces of ice. The idea is to identify the vertical frequencies of the region by performing a vertical Fourier transform on blocks. Then by identifying the frequency with the highest amplitude we can separate the different pieces of ice from the water. As this frequency is link to the rotational speed, with a well chosen Fourier sampling (zero padding on each blocks of the image) we can distinguish the iceberg from the other parts. Two problems appear with using this solution. First the relief on the iceberg affects the fringes, they are not homogeneously horizontal especially on elevated region (cf *fig. 10*), this causes discontinuity on the result. Secondly, it appears that the noisy water is not as blank as expected. This method found some correlation on the vertical frequency of the water and regions seems to appear with a constant main vertical frequency.

The previous solution was not convincing, so we tried something else. It appeared that the amplitude signal was appropriate for a region growing algorithm, the grey level of the iceberg was indeed much different than those of surrounding water and ice. This important amplitude difference between the iceberg and floating ice is most probably due to the composition of the ice: the iceberg comes from the glacier and is composed of fresh water whereas pieces of ice are salty frozen water. The goal of the region growing algorithm is to define an inside and an outside, it is a recursive process. First, it needs a starting point which has to be inside the region, it is the seed. In each loop every pixel that are neighbouring the

region are tested: if the new region (the previous region + the neighbouring pixel) keeps its weight inside the Growing Condition (GC) then the pixel is now part of the region, if no neighbouring pixel satisfy the GC then the algorithm stop and the region is returned. The region growing algorithm can be seen as follow:

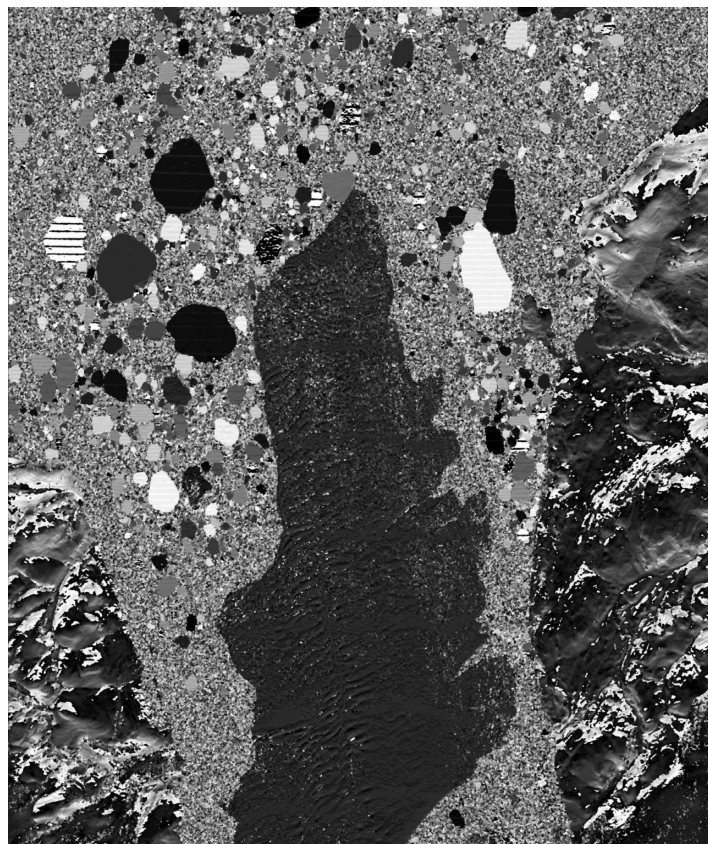
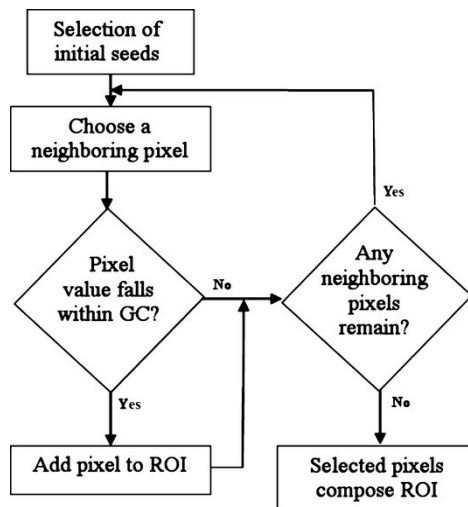


Figure 10. Result of the vertical block Fourier transform algorithm with 30 sampling levels. We can spot the artefacts on the iceberg and the scattered block of water.

ROI is the region of interest. The condition we chose for the region growing is the max-min, we impose at the beginning of the algorithm a tolerance threshold and if the pixel fall into $\{ \text{mean}(\text{region}) - \text{threshold} ; \text{mean}(\text{region}) + \text{threshold} \}$ then it is accepted. This criteria was preferred to an order two because it can easily grow at the beginning, the mean is very volatile, and stabilise as the region get wider. The threshold remains a critical variable in this algorithm, if we rise the threshold, unwanted area will be accepted inside the region. If the threshold is too low, the region will be cut because of a slight different level, parts of the glacier will not be selected. To get rid of the inside noise, we run another region growing with this time the seed outside the iceberg, so that we get an inside-out filled up area. The detail to take care here is the border, it can easily be ripped out. Our solution was to smooth the result in order to widen the area of interest. On *fig. 11* we can see the result of the region growing algorithm.

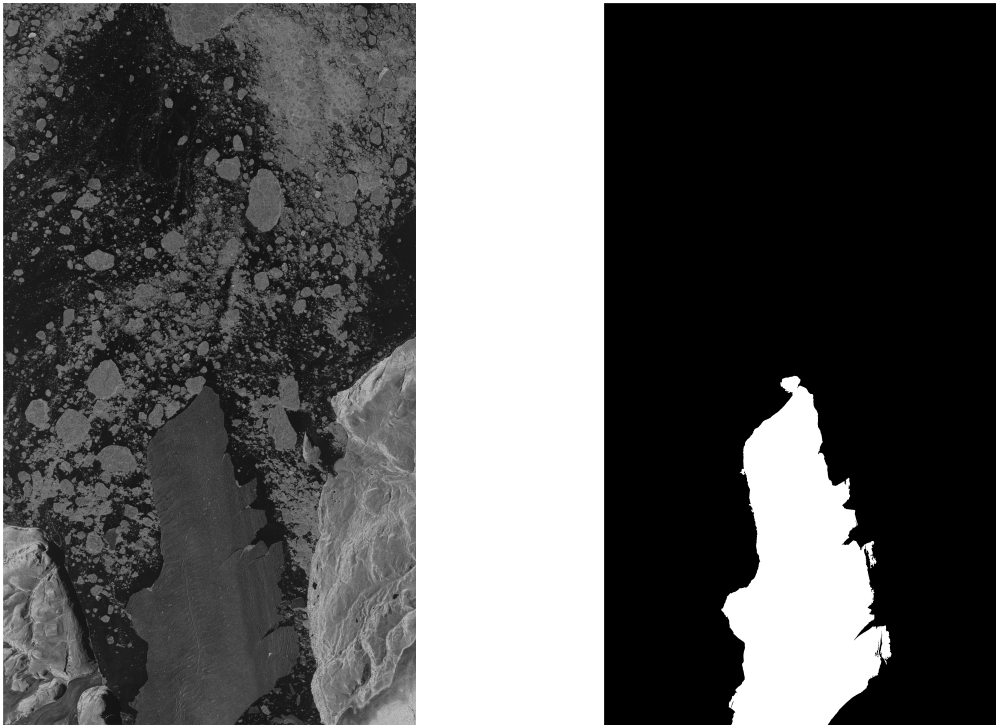


Figure 11. Result of the region growing algorithm in slant range azimuth coordinates. Left: amplitude image, right: region isolated. There is still some artefacts on the right part of the iceberg, also one piece of ice on the top should not be in the region

III.2.2. Removing fringes

We saw in the theoretical part about interferometry that rotation motion of the target lead to fringes which will disturb the DEM production, especially the phase unwrapping. In order to get rid of these artefacts, we applied a demodulation on the masked phase image. After masking the phase with the region growing result, we extract the vertical Fourier transform of the phase, extract the frequency which has the more amplitude and then demodulate. The demodulation in itself is done by transforming the phase image into a complex signal and then multiplying it by another complex signal which phase is a one incremented vertical slope multiplied by the frequency found previously.

$$\text{Demodulated image} = \arctan(\exp(j.2\pi \cdot \text{phase} \cdot \text{vertical slope} \cdot \text{frequency})) \quad (14)$$

The huge size of the iceberg made it even possible to remove the fringes even without the masking step. However it is a bit risky, the result can be all wrong in case there is a more dominant vertical frequency. On the *fig. 12* we show that the result are still correct.

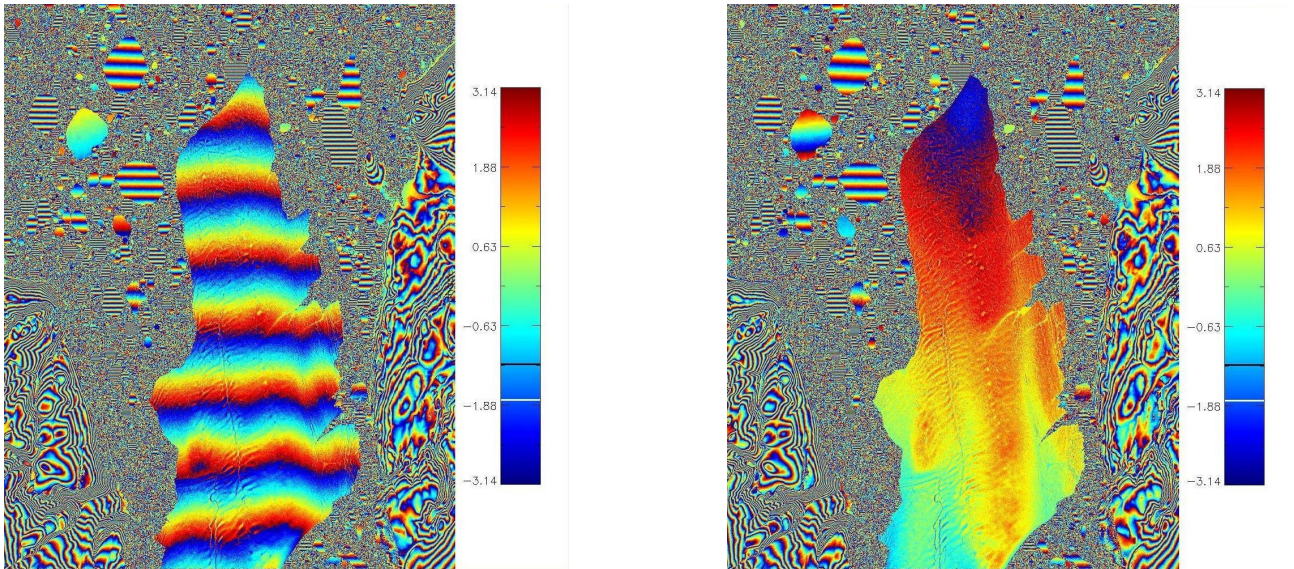


Figure 12. The fringes removing gives correct result even without the phase masking. Left: phase image with the fringes, right: phase without the fringes. Those images are still in slant range azimuth coordinates.

Now that the interferometric images are ready for the phase unwrapping we can produce the geocoded DEMs with the TAXI program. With the water removing, the processing time is down to about three hours for each production from three days and we don't have the slope artefacts due to the rotation, the benefits are sizeable. With the geocoding, we now have square corresponding pixels of 10x10m, However the height accuracy remains different between all those data, this is mostly due to the different baselines between the acquisitions. The important drawback is that we had to cut the images with the region growing and therefore we lost some information on the edges. Let us have a look at the geocoded iceberg DEMs, TAXI gave us all the coordinates so we can plot them on a latitude against longitude chart. Here is on *fig. 13* all the DEMs plotted on the google earth globe with the relevant data.

III.3. Estimation of the rotation

In order to spot the surface differences between all the acquisitions we first have to align them on the same grid. The objective in this phase is to reach a sub-pixel accuracy that will allow us to identify the melting and carving. The drifting of the iceberg will be identified by cross-correlation, using the property of the Fourier transform we just need to multiply in the Fourier domain. We should keep in mind that with a






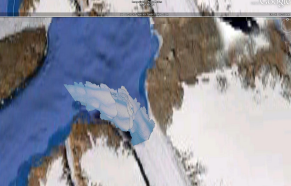



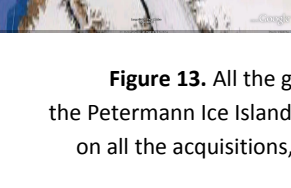
|  | N° | Date | Hour | Scene | Baseline (m) | Height of ambiguity(m) |
|---|----|------------|----------|-------|--------------|------------------------|
|  | 1 | 25/08/2010 | 20:44:09 | 3 | 193.852 | 40.4465 |
|  | 2 | 31/08/2010 | 20:35:32 | 5 | 184.108 | 39.1820 |
|  | 3 | 02/09/2010 | 20:01:13 | 6 | 148.644 | 33.8765 |
|  | 4 | 03/09/2010 | 11:53:51 | 2 | 169.293 | 38.0833 |
|  | 5 | 05/09/2010 | 20:44:09 | 3 | 197.069 | 39.7939 |
|  | 6 | 08/09/2010 | 19:52:38 | 4 | 137.901 | 33.2327 |
|  | 7 | 11/09/2010 | 20:35:32 | 5 | 186.814 | 38.6142 |
|  | 8 | 13/09/2010 | 20:01:13 | 6 | 149.382 | 33.7047 |
|  | 9 | 14/09/2010 | 11:53:51 | 2 | 169.347 | 38.2969 |

Figure 13. All the geocoded DEMs plotted in chronological order on the Google Earth globe, the drifting and rotation of the Petermann Ice Island is obvious. The tenth acquisition did not capture the iceberg. The iceberg is not completely acquired on all the acquisitions, moreover it broke in half between the 8th and the 11th of September. This shape modification will perturb the alignment process.

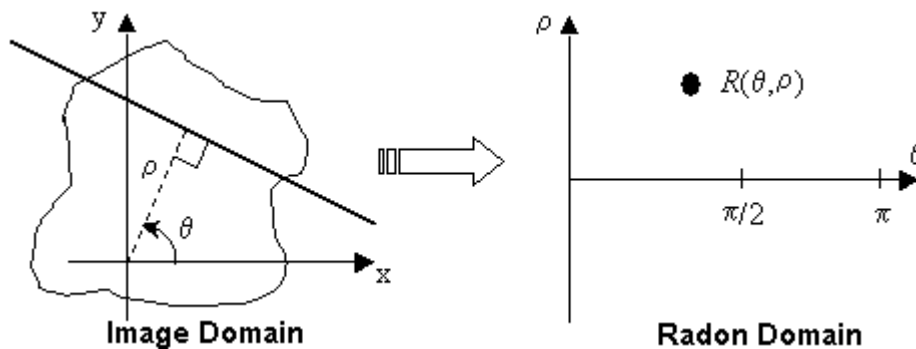
10x10m² resolution the DEMs are roughly contained in a 3000x3000 pixels image. At this size, even a simple FFT take some time. A cross-correlation in this condition takes around 1 minute to execute.

$$\text{Drifting vector} = \max(\text{FFT}^{-1}[\text{FFT}(\text{image 1}) \times \overline{\text{FFT}(\text{image 2})}]) \quad (15)$$

As the iceberg is almost flat and possess only few specific features it is sometime more effective to cross-correlate the slope instead of the altitude in order to improve the details, this technique was mostly used in the case of an important shape difference. To get the slope, we applied a Sobel filter on the DEMs images. This compensation of the drifting was applied between each rotational identification. Rotation is a bigger problem than the drifting. Indeed, inSAR specialists are not use to deal with such wide rotation, usually the rotations which are processed in SAR field are below the 5° angle and they are solved by using the Block Correlation technique. This technique excel in identifying small angles. For this problem we will have to use another image process, the radon transform. Each of these methods had to be used multiple time in a row in the case of difficult data. The shifting between each try usually improves drastically the outcome.

III.3.1. Radon process

The radon transform is a mathematical transform mostly used in biomedical imagery. The new domain is defined by the coordinates ρ and θ and the value of the $R(\theta, \rho)$ pixel is the value of the integral of all the pixel values located on a line distant by ρ from the centre point and leaning by θ . This transform was created in order to deal with the cross-sectionnals scans of tomography. Images in the Radon domain are called sinogram because the transform of the Dirac function gives a sine distribution.



This transform is helpful here because of his rotational properties. Indeed, if the object in the image domain is rotated by an angle α around the centre point it will result in a sinogram translated by α in the angular dimension. Thus we have to first centre the images, then switch them to their respective radon correspondent and finally find the one dimensional translation vector by cross-correlation. The centring is performed by a barycentre calculation in order to centre this point. Due to poor radon implementation on IDL, we had to adapt the algorithm with a Hanning windowing to reduce edge effects.

Results of this step rely a lot on the shape of the acquisition, on similar shaped iceberg the radon process gave us good results. They were significantly worse in the case of a cut acquisition or after the

second splitting. The results found by this process were tested using a block correlation technique we will explain in the next point.

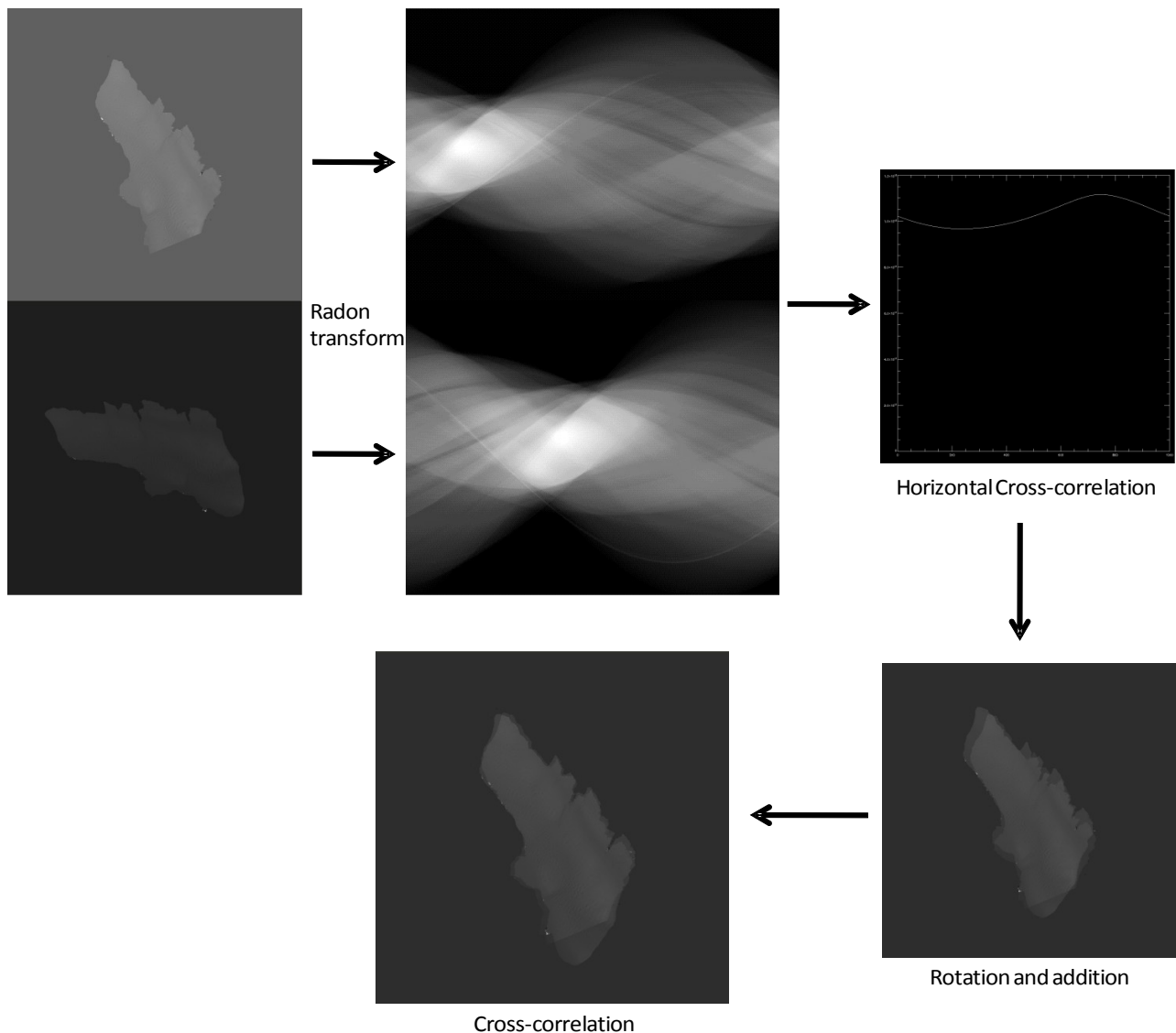
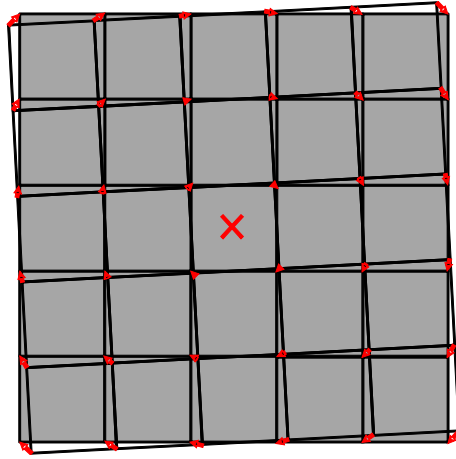


Figure 14. Visualisation of the steps of the radon process starting with centred DEMs.

III.3.2. Block correlation

Now that we have both the DEMs centred and within a small angle we can apply the block correlation, technique usually applied for this problem in radar domain. The theory of this algorithm lies on small rotation approximation. In the case of a small angle rotation, the displacement of each block of the image can be seen as a translation, the following figure show this approximation. Thus we can rely on the now classic cross-correlation in order to find all these vectors. Those vectors can give us the angle of rotation by trigonometry, nevertheless we need the coordinates of the centre of rotation. By calculating one angle by block and taking the mean of the sum we can have a good approximation of the rotation angle.



The first step of the Block Correlation process is to shred the two images into small blocks. Then we perform a cross-correlation between each correspondent block of both images. The size of the block limits the precision of the estimation: with small boxes there is a lot of angle values therefore a better approximation, but for blocks far from the centre of rotation the displacement is too important, the blocks are not stacking up and the cross-correlation fails. The top right image of the figure 15 display the length of the translations for each block. Now that we have all the drifting lengths we must isolate the region where the cross-correlation was relevant from the region where the blocks were apart. This region is surrounding the centre of rotation, its range depends on the size of the blocks and the angle of rotation. In order to calculate the angle only on those pixels, we used the relative value of the cross-correlation. The idea we have is that if the blocks are stacking and that the correlation is relevant then the value of this correlation should be high compared to blocks where there is no relation. On the top right of figure 15 there is the image of the relative correlation values, we can spot a common position between the contiguous region on the left and the high correlation values on the right. In order to only select this highly correlated region we had to apply once again a segmentation algorithm. The difference between relevant and irrelevant correlations is here not visually very obvious, the segmentation process was arduous. We used the region growing described in the previous part, but here some pre-processing on the correlation values were needed. First, as we can see on the top left of the figure 15, the edges of the glacier remains very noisy, so we removed them using a Sobel filter. Then we applied a smooth filtering on the values before using our Region Growing algorithm. The seed is selected on the centre of rotation and the threshold has to be carefully chosen. On the bottom right of the figure 3, we display the result of the segmentation, a lot of the original contiguous region has been cut out and some other noisy part has been accepted in. The result is not perfect but with the averaging on the result we obtained a satisfying angle estimation.

The angles are calculated by trigonometry. As we know the centre of rotation, the coordinate of the pixel and the distance it moved, we can simply apply the small angle approximation and basic trigonometry so that we obtain the angle θ .

$$\theta = \arccos\left(1 - \frac{V}{\sqrt{2}R}\right) \quad (16)$$

With V the distance of displacement and R the distance to the centre of rotation.

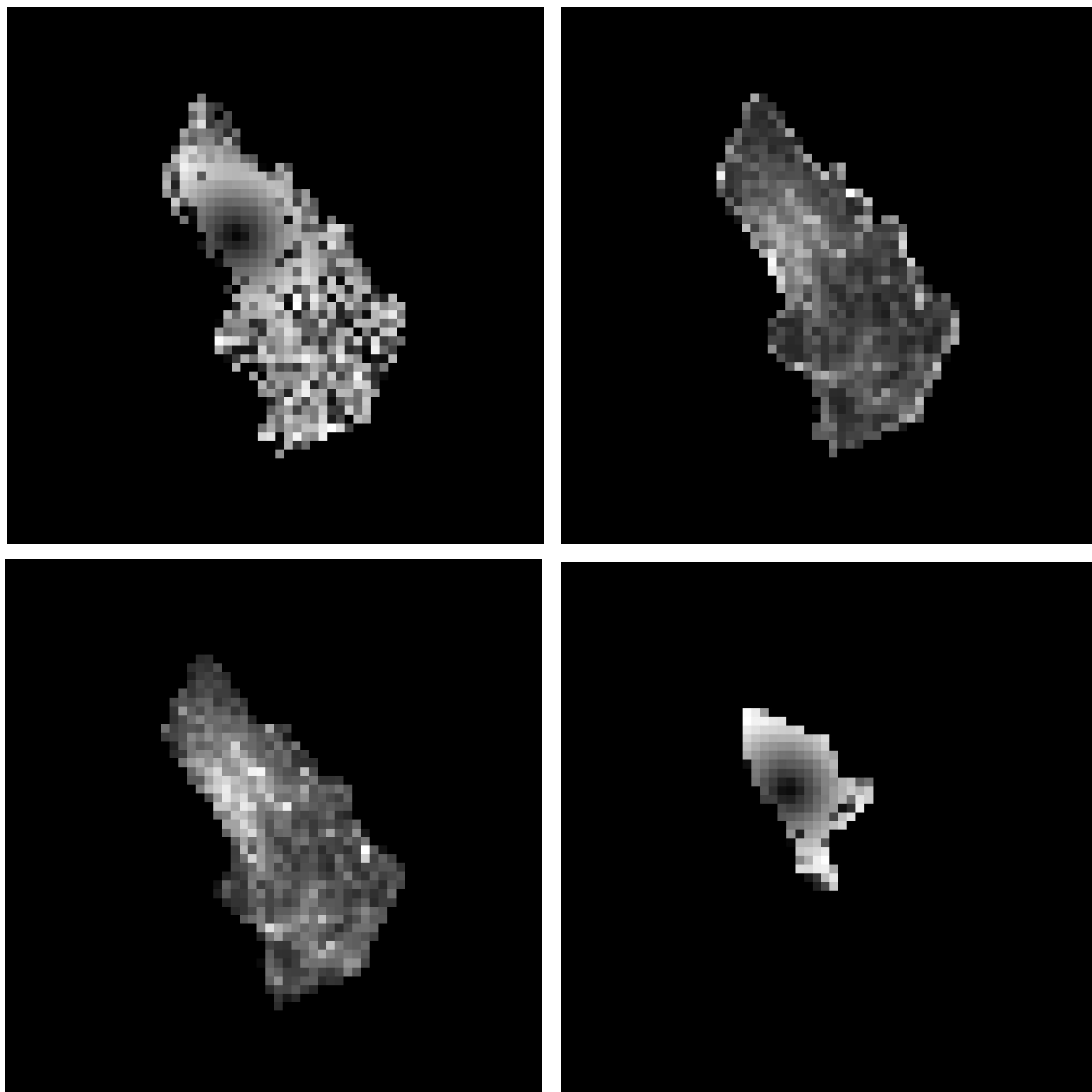


Figure 15. The output of the block correlation with blocks 64 pixels long. Top left: length of the translations between the block, the relevant region around the centre of rotation is obvious. Top right: relative values of the cross-correlation. Bottom left: removing the edges. Bottom right: length of the relevant translations selected by the segmentation process, with those value we can estimate the angle of rotation.

In order to check our result, we perform a new block correlation to identify any remaining rotation. This time, as we expect a much smaller angle, we can reduce the size of the blocks to spot precisely any misalignment. The Block Correlation process usually has to be performed multiple time, each time it improves the alignment. The figure 16 displays the result of the whole sequence of alignment and its last Block Correlation with a very small block size.

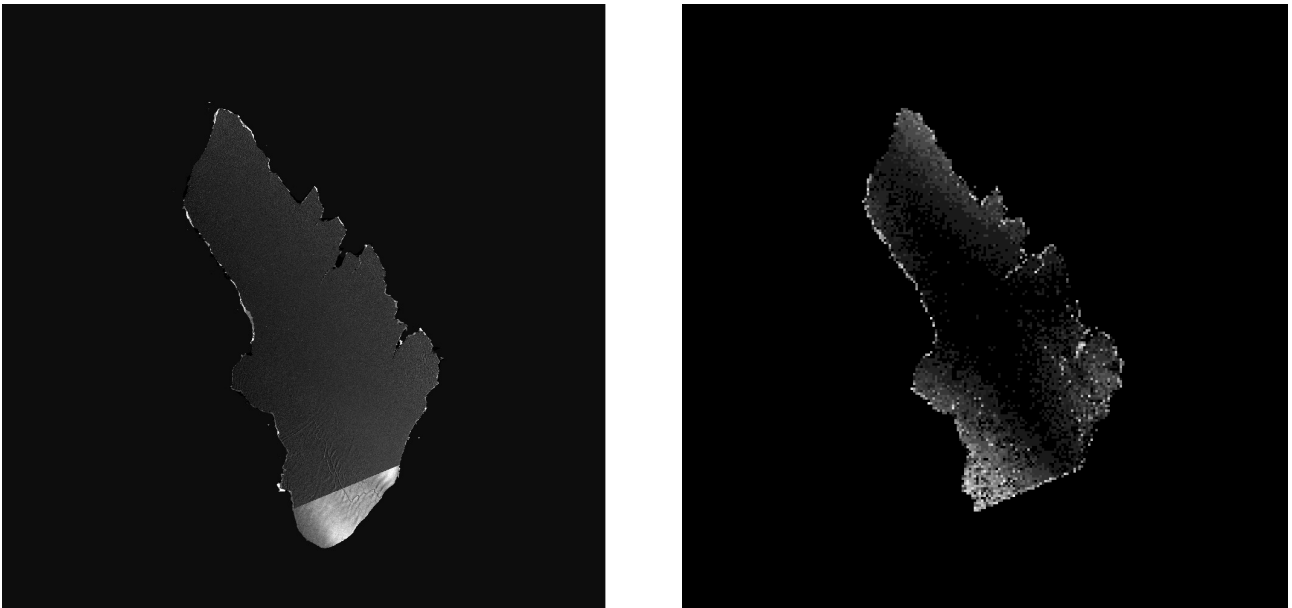


Figure 16. Result of the entire Block Correlation recursive process. Left: Subtraction of the two aligned DEMs. Right: Length of displacement, output of the last Block Correlation with 16 pixel sized blocks. We can not identify the typical rotation pattern seen previously.

III.4. Surface monitoring

At this step of the process we have stacking geocoded DEMs which share the same pixel resolution. There are still differences remaining between those data, they are mostly due to the different acquisition locations: the baseline (and so the height of ambiguity) modify the accuracy between acquisitions, the inclination (due to flat earth approximation) adds a geometrical artefact on uneven surfaces and the time of the day (with the partial melting of the surface ice) impact the DEM result. Those accuracy alterations are unfortunately impossible to remove now, it would require much information on the area, for example knowing some ice properties and the temperature of the ice at the moment of acquisition. To monitor the iceberg's surface modifications we will postulate that it is still possible despite this deficit of knowledge. As the DEMs are relative, we had to eliminate the mean difference between each image. Unfortunately, due to lack of time we could not implemented a slope correction, we did not think in the conception phase that the iceberg would have a mean slope evolution. Moreover this problem could only be pointed out after seeing the ending results and therefore executing the whole chain of process.

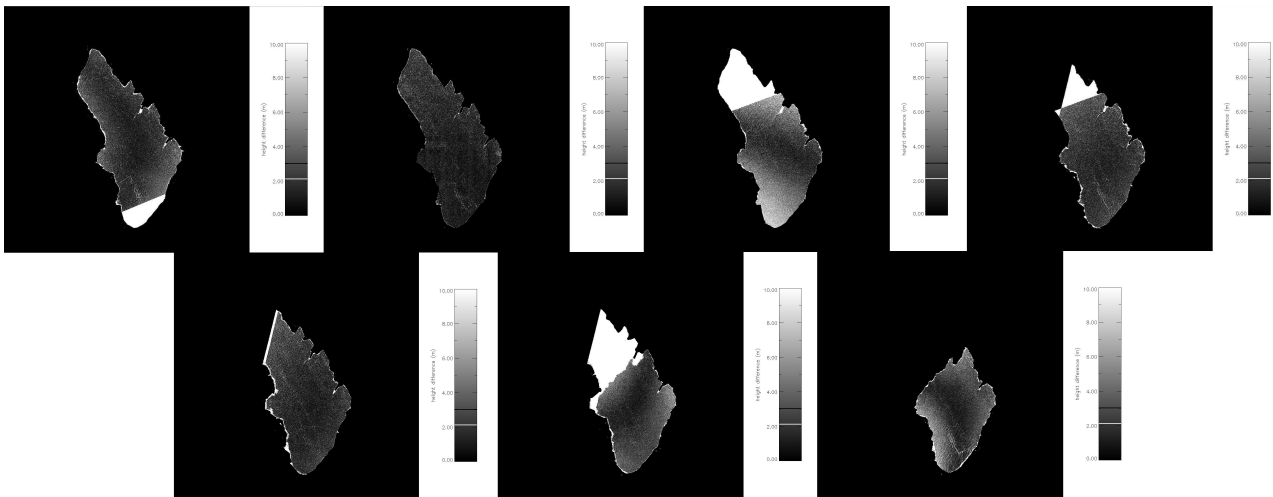


Figure 17. Monitoring the surface evolution in chronological order. We have here the absolute value of the subtraction between each consecutive DEM. We have only 7 evolutions for 9 DEMs because the last DEM had a very cut shape, the alignment process did not fulfil. We can see on some of them that the slope effect is obvious (especially the 4th), however a mysterious curvy artefact appeared.

The evolution is spotted by subtracting each temporal consecutive DEMs. The figure 17 shows the result we obtained. The quality of the alignment can be visually measured on this result: for only one pixel translation, subtraction of the surface's features can be constructive or destructive, same thing with a tiny rotation. We are quite satisfied with the sub-pixel alignment we achieved here. On these results we can easily observe a slope effect, indeed there is almost always a line of zero height differences separating two more distant area. This slope effect ruins almost all our monitoring. Yet another artefact worth noticing, sometime the line of zero height difference is curvy, especially on the first and last evolutions of *fig. 17*. The origin of this curve has not been ascertain. It maybe comes from the alterations described previously or it is maybe just due to the melting in addition of a slope.

Conclusion

The conclusion of this project is both disappointing and satisfying. Disappointing because of the slope we did not predict and which annihilate our evolution monitoring. In a way, it is quite astonishing to observe such high slope between two consecutive acquisitions. Two reasons were found to explain this high value, first the iceberg started drifting heavily just after our initial acquisition, it got stuck on a rock between the 31st of August and the 11th of September (almost all the acquisition span). It is possible that the iceberg leaned seriously during this period because of the pressure induced by the water current. The second reason is linked to our algorithm which removes the rotational fringes, the sampling of the frequency during the Fourier transform can lead to estimation mistakes, wide fringes can remain and therefore a mean slope subsists. Whatever the case, this slope removing could be performed with a gradient multiplication. If we achieve identifying the slope (that can be done by interpolating the heights), we can apply a gradient in the slope direction but with an opposite amplitude in order to compensate the effect.

But the aftermath of the project are also gratifying. Indeed, if we omit the slope, the whole process is working smoothly. The pre-processing steps improve greatly the processing time while they are solidly performing their tasks. In the same way, the post-process fulfil its task with decent results. Moreover, even with the sensitive InSAR processing we achieve to process some interesting results. We worked during this project with astonishing piece of data, the images acquired by TanDEM-X are amazingly precise. It is very satisfying to know that this project will be followed by the work of Jose Garcia Molina.

Despite the complexity of SAR and InSAR theories it is very gratifying to understand how they are constituted and to apply directly your knowledge by implementing image algorithms. Dealing with radar images which have a strong physical emphasis can be at first surprisingly different than optical images. Satellite imagery remains a wide field of study where a lot of scientific domains are meeting, robotic, telecommunication, space engineering and signal processing are only some examples. The German space centre can be proud to possess such prolific minds that realised this project, and I am glad to have work with them for six months.

Thanks:

To Paco Lopez-Dekker for all the time and explanations he granted me, to Francesco De Zan for his precise InSAR knowledge and his help on IDL, to Pau Prats for his vital help dealing with TAXI and InSAR process, to Steffen Wollstadt for his time and logistical help, to Gehrard Krieger for his expertise on the problem, to the whole Microwaves and Radar Institutes which grants me a warm welcome inside its team.

References:

- [1] J. Allen and R. Simmon, "Ice Island Calves off Petermann Glacier", <http://www1.nasa.gov/topics/earth/features/petermann-calve.html>
- [2] T. Fritz, M. Eineder, "TerraSAR-X ground segment basic product specification document", **Cluster applied remote sensing, issue 1.7, 15.10.2010**
- [3] G. Krieger, A. Moreira, H. Fiedler, I. Hajnsek, M. Werner, M. Younis and M. Zink, "TanDEM-X: A satellite Formation for high-resolution SAR interferometry", **IEEE Transactions on Geoscience and Remote Sensing, VOL. 45, NO. 11, November 2007**
- [4] P. Prats, M. Rodriguez-Cassola, L. Marotti, M. Naninni, S. Wollstadt, D. Schulze, N. Tous-Ramon, M. Younis, G. Krieger, and A. Reigber, "TAXI: a versatile processing chain for experimental TanDEM-X product evaluation", **Microwaves and Radar Institute German Aerospace Center**
- [5][12]: D. Massonet and J.C. Souyris, "Imaging with Synthetic Aperture Radar", **2008**
- [6][11][13][15]: P. Prats, "Airborne Differential SAR Interferometry," **Ph.D. dissertation, Universitat Politècnica de Catalunya, Dept. of Signal Theory and Communications, Barcelona, Spain, Feb. 2006**
- [7] Graham L.C., "Synthetic interferometer radar for topographic mapping", **Proc. IEEE 1974 vol. 62 763**
- [8] Gabriel A.K. and Goldstein R.M., "Crossed orbit interferometry; theory and experimental results from SIR-B" **Int. J. Remote Sens. 1988 vol. 9 857**
- [9] Gabriel A.K., Goldstein R.M. and Zebker H.A., "Mapping small elevation changes over large areas: differential radar interferometry" **J. Geophys. Res. 1989 vol. 94 9183-91**
- [10] "Special section on spaceborne radar for earth and planetary observations" **Proc. IEEE vol. 79 773**
- [14] Stanford Radar Interferometry Research Group, "SNAPHU: Statistical-Cost, Network-Flow Algorithm for Phase Unwrapping", http://www-star.stanford.edu/sar_group/snaphu/
- [16] P. Lopez-Dekker, P. Prats, F. De Zan, D. Schulze, G. Krieger and A. Moreira, "TanDEM-X first DEM acquisition: a crossing orbit experiment" **IEEE Transactions on Geoscience and Remote Sensing, VOL. 8, NO. 5, September 2011**